FAKULTA MECHATRONIKY,
INFORMATIKY A MEZIOBOROVÝCH
STUDIÍ TUL

Dissertation thesis summary

Single-snapshot compressive hyperspectral imaging using coded aperture

Studijní program: P3901 Aplikované vědy v inženýrství
Studijní obor: Aplikované vědy v inženýrství

Autor práce: **Ing. Jiří Hlubuček**
Školitel práce: RNDr. Karel Žídek, Ph.D.
Ústav nových technologií a aplikované informatiky

Liberec 2022

Annotation

This thesis presents a novel approach to the remote detection of chemical information by compressing the hyperspectral information directly during the measurement. This was enabled thanks to a novel technique developed on a single snapshot called coded aperture snapshot spectral imaging (CASSI). Using a coded aperture allows the implementation of a modern signal processing technique based on an algorithmic strategy – compressed sensing. This method can capture complete hyperspectral information in a single instance without scanning, which yields a significantly higher optical throughput compared to its scanning-based counterparts. By using the CASSI system, it is possible to retrieve the information faster than by a traditional system, using a relatively simple optical setup. In this thesis, the method was extended in order to perform hyperspectral imaging on a broad spectral range in the infrared region.

Keywords: hyperspectral imaging, compressed sensing, coded aperture

Anotace

Tato práce představuje nový způsob získání chemické informace na dálku s kompresí hyperspektrální datakrychle přímo v průběhu měření. Toho je docíleno díky nové technice založené na jediném snímku z detektoru, tak zvané CASSI (Coded Aperture Snapshot Spectral Imaging). Kódovaná apertura umožňuje implementovat moderní techniku zpracování signálu s použitím algoritmu – komprimované snímání. Tato metoda je schopna zachytit kompletní hyperspektrální informaci v jediný okamžik bez nutnosti skenování a dosahuje daleko větší optické propustnosti než její standardní, na skenování založené protějšky. Použitím CASSI je možné získat měřenou informaci rychleji než pomocí tradičních systémů, s použitím relativně jednoduchého optického uspořádání. V této práci byla CASSI metoda vylepšena pro možnost hyperspektrálního zobrazování na širokém spektrálním rozsahu v oblasti infračerveného spektra.

Klíčová slova: hyperspektrální zobrazování, komprimované snímání, kódovaná apertura

Contents

List of Abbreviations

CASSI	**C**oded **A**perture **S**napshot **S**pectral **I**maging
CR	**C**ompression **R**atio
CS	**C**ompressed **S**ensing
D-CASSI	**D**ifferential **CASSI**
DCT	**D**iscrete **C**osine **T**ransform
DMD	**D**igital **M**icromirror **D**evice
FO	**F**irst **O**rder
HDES	**H**yperspectral **DE**tection **S**ystem
HS	**H**yper**S**pectral
HSI	**H**yper**S**pectral **I**maging
IR	**I**nfra**R**ed
LWIR	**L**ong-**W**ave **I**nfra**R**ed
MIR	**M**id-**I**nfra**R**ed
NIR	**N**ear-**I**nfra**R**ed
PSNR	**P**eak **S**ignal-to-**N**oise **R**atio
SAM	**S**pectral **A**ngle **M**apper
SNR	**S**ignal-to-**N**oise **R**atio
SSIM	**S**tructural **SIM**ilarity
TwIST	**Tw**o-step **I**terative **S**hrinkage/**T**hresholding algorithm
VIS	**VIS**ible
ZO	**Z**eroth **O**rder

Introduction

Our vision is an extraordinarily complex and astonishing system, and we depend on it as a primary source of gathering information about our surroundings. Nevertheless, it has limitations in imaging very tiny or distant objects, and we are constricted only to three spectral channels in the visible spectra. Observing nature and developing optical systems over the centuries taught us that there is always something new to discover and far more information around us than we are able to grasp with our senses, whether it is gravitational waves or trillions of neutrinos permeating you at this very second. In fact, the amount of information around us is so vast that for the human brain to process it, it is designed to filter even the limited visual data captured by our eyes. Seeing broad spectral range, e.g., in the infrared (IR) region with fine spectral resolution would allow us to remotely sense chemical composition [1]. This is what hyperspectral imaging (HSI) does. HSI denotes methods that are able to capture both an image and a spectrum of light in each pixel of the scene. Such a dataset provides us with immense information about the measured scene, which cannot be obtained by any other means. Therefore, IR HSI has been a very lively topic in the last decades [1, 2, 3, 4, 5].

Within this field, most studies are focused on the near IR spectral region because it is possible to use common optical elements and germanium detectors or detectors on an InGaAs basis. However, the implementation of HSI in the middle and far IR spectral region is problematic due to the need to use "exotic" optical materials and detectors with high noise levels. HSI is very demanding regarding the acquisition time, computing power, processing, and storing the information. Moreover, in conventional signal processing, one is limited by the Nyquist-Shannon sampling theorem, which states that in order to reconstruct a signal faithfully, the sampling frequency must be at least twice as large as the highest frequency in the signal [6].

A possible solution to these problems is utilizing the compressed sensing (CS) method [7]. It is possible to reconstruct a sparse signal sampled at a rate less than the one restricted by the Nyquist-Shannon criterion through constrained l_1 minimization [8]. This approach was used in the 1970s in reflection seismology for constructing images of layers within the earth [9]. CS is invaluable for cases where there is a need to acquire huge datasets, such as in HSI. An impressive demonstration of the acquisition of an extensive amount of data and the CS uniqueness can be found in [10], where the authors were able to attain as many as 70 trillion frames per second. One of the methods that combine HSI with CS techniques is the so-called CASSI (Coded Aperture Snapshot Spectral Imaging) [11, 12, 13]. The CASSI technique is the central method of this thesis.

The two main components of the CASSI setup are a dispersive element and a coded aperture, which is a random pattern – typically a binary one. The random pattern, or in other words, a random mask, encodes the image information for every wavelength and a dispersive element shears the image spectrally on the detector. The resulting image is then used for reconstructing the hyperspectral information back. The unique advantage of CASSI is it does not need to scan the scene. All the hyperspectral data are captured in a single instance. However, since the CASSI method relies on one snapshot on a detector, the compression of the

hyperspectral data is enormous. This limits the use of this method on a small number of spectral slices, which often implies the acquisition of a narrow bandwidth [12, 14]. Hence, an improvement of this method is on the spot.

This thesis describes our aim to improve the potential of the CASSI method by using various approaches to improve the compression ratio and reconstruction quality. The approaches are evaluated both in an experimental way and in realistic simulations, which test their utilization for the IR HSI.

The first chapter is devoted to the theoretical fundamentals necessary to understand the experimental part of this thesis. The second chapter provides an overview of the state of the art and applications. Also, there are mentioned objectives of this work. From the third chapter onward, starts the experimental part of my work. This includes characterization of our optical system, data processing, and reconstruction. Chapters 4, 5, 6, and 7 describe the modifications of CASSI and evaluate the utilization of the method in the IR spectral region. Chapters 4-6 also give more insight into the articles I have written and are attached at the end of this thesis. The results in Chapter 7, exploring the potential of an enhanced CASSI system for IR HSI, are yet to be published. Chapter 8 summarizes the work carried out within the thesis.

For the reference purposes, in this thesis summary, I keep the same numbering of the main chapters as in the thesis. Figures, Tables, and Equations are denoted here with capital letter S.

1 Theory: the pieces of the puzzle

In the thesis, this chapter is devoted to the essential aspects needed to understand the CASSI technique, which I have been using throughout the thesis. It begins with a brief description of hyperspectral (HS) imaging with a focus on the infrared (IR) spectral region. It continues with an introduction to compressed sensing and the associated method CASSI, showing the fundamentals, characteristics, and limitations. Finally, it presents metrics to assess the HS datacube quality.

2 State of the art

2.1 Current challenges in hyperspectral imaging

In contrast to the standard RGB imaging, by hyperspectral imaging (HSI), we obtain spectral information in addition to the 2D image. The spectral information can be exploited in various ways – for instance, to identify the chemical composition. From the principle of this method, it is evident that one acquires a massive amount of information (see Chapter 1.1 in the thesis). This naturally affects the acquisition times, which could be in the order of seconds to hours to acquire the complete information, depending on the required spatial and spectral resolution and the method used [15].

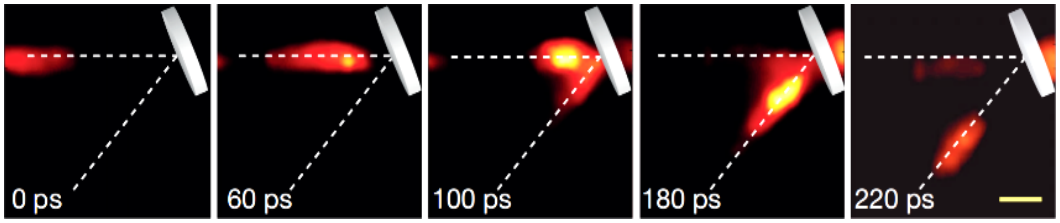

Figure S1 Photos of a laser pulse being reflected on a mirror, scale 10 mm. Adapted from [18]

An integral part of most hyperspectral instruments is the moving part required to scan the imaging scene, which is one aspect of the complexity of these instruments. It is also necessary to mention the low efficiency of radiation utilization. For example, in a line scan, a large part of the light intensity is filtered out by the slit used, or in a plane scan, the light is filtered out using a narrow bandpass filter. So, the better the spectral resolution one wants, the worse the use of light is.

Recording, storing, and processing hyperspectral information is very demanding in terms of acquisition time, storage capacity, and computing power. For example, in the realm of earth remote sensing, there are freely accessible data from the AVIRIS instrument [16]. It is an optical sensor that provides calibrated images of the spectral radiance in 224 spectral channels. Typically, the file size of these data is several GB. Therefore, the traditional classification techniques cannot be directly applied to the HS data, and modification is needed [17]. In addition, the need for using complex optics, and thereby the high purchase price, plays a role here.

Moreover, as we measure a scene pixel by pixel for very fast phenomena, we are limited by the acquisition time. A possible solution to most of these problems is the use of compressed sensing techniques, specifically the CASSI method (see Chapter 1.4 in the thesis). For example, Gao et al. [18] accomplished to capture events happening on the order of tens of ps – a reflection of a laser pulse on a mirror (Figure S1).

2.2 CASSI

Thanks to CASSI, one does not need to scan the scene because the method is based on only one image from the camera, i.e., a single snapshot. It is captured in a single moment, and this image is much smaller in size than the entire hyperspectral datacube. Then it is possible to reconstruct the scene back thanks to the knowledge of the random mask and that common images are sparse. A random mask is a binary pattern resembling QR code (see Figure S2). By not having to use a slit or narrow bandpass filters as in the standard hyperspectral approaches (see Chapter 1.1 in the thesis), the utilization of light is significantly improved, which is absolutely critical for real-world applications. Also, naturally, there are no scanning artifacts. In Fourier-transform infrared spectroscopy, the optical throughput gained compared to the standard spectrometers using slits is called the Jacquinot advantage [19]. Similarly, using snapshot imaging in HSI, the throughput improvement in comparison to the scanning-based systems is referred to as the snapshot advantage [20].

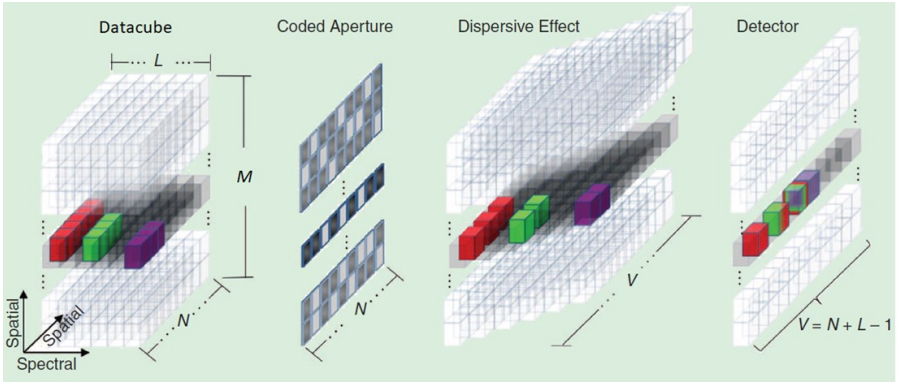

Figure S2 An illustration of the spectral optical flow in CASSI and an example of a QR code resembling random mask pattern. Adapted from [13]

However, for a wide spectral range, taking only one snapshot brings in a large compression between the data recorded on the detector and the hyperspectral datacube we want to reconstruct. This issue is typically overcome by limiting the sensing to a narrow spectral width (100-190 nm) [12, 14], which is discretized to a relatively small number of wavelength regions (25-28 spectral slices). It is, in fact, very counterproductive. For example, if we are trying to detect the absorption spectrum of a chemical substance, we need a much finer wavelength resolution for its characterization. For instance, measuring on a spectral range of 8-14 μm, 28 spectral slices would provide a resolution of only approximately 214 nm. In this way, any sharp absorption peaks of a chemical compound would be undetected. The standard CASSI also exhibits limitations in image quality for complex scenes and the time needed for the hyperspectral datacube retrieval, which can reach as long as 14 minutes [12] since the reconstruction problem is severely underdetermined.

Attempts to improve the reconstruction quality and the compression ratio are usually implemented using multiple snapshots of the same scene [21, 22, 23, 24, 25], while some of them also try to optimize the coded aperture [23, 24, 25]. But then, the CASSI method loses its uniqueness in recording the hyperspectral data in one instance. Moreover, some advanced modulator to change the random mask pattern is required, or the optimized masks are spectrally selective. There was also an effort to use a higher-order discretization model image for reconstruction [26]. However, the used complex model describing the detector increases the computational demands highly, as it calculates with 170 spectral bands instead of 8.

A promising way to enhance the CASSI performance is to capture a non-diffracted image of a scene that provides more knowledge about the measured scene [14, 27, 28, 29, 30]. Nevertheless, attaining the non-diffracted image requires splitting an incoming beam, and a second detector is needed, which makes the optical system even more complex. The light splitting can reach as much as 50% intensity loss in the measured spectrally sheared image [27].

In addition, due to the use of a random mask that encodes the image for each wavelength, the imaging quality of the system is critical in the whole measured spectral range. It is needed to attain the image without distortion or chromatic aberration to obtain good-quality reconstruction in the standard CASSI experiment. Otherwise, these discrepancies would lead to wrongly encoded information, and it would subsequently cause problems in reconstruction. It is easily feasible in the visible spectral region, where various complex lenses corrected for aberrations are available off-the-shelf. However, in the IR spectral region, this is more challenging. Complex IR optical systems are costly, and their adjustment is highly demanding.

Another criterion, which is essential for using CS in HSI, is the time required to reconstruct hyperspectral data. This information is usually intentionally not stated in the literature. An example of a rare case where the computational times are present is Ref. [12]. Here the authors declare that for 100 iterations of the reconstruction algorithm, a time of 14 minutes on a desktop PC was required (datacube with dimensions of 128×128×28 pixels, spectral range 540-640 nm). The authors do not explicitly state how many iterations were needed for the overall data reconstruction. Nevertheless, assuming the reconstruction was restricted to 100 iterations, the time required is still not suitable for real-life processing. The same group in Ref. [31] demonstrated the ability to capture 248×248×33 datacubes at video rates (30 fps). The catch is that the postprocessing took several hours of computing time to reproduce the video datacube sequence.

Based on the above-listed shortcomings, Chapter 2.4 sets out the objectives of this thesis.

2.3 Application of HSI and CS

In this chapter, only a few selected applications of hyperspectral imaging and compressed sensing will be mentioned. Since these are very broad topics ranging from agriculture to medical applications, it highly exceeds the scope of this work.

Thanks to the conventional HSI, it is possible to noninvasively determine the quality of food [5, 32] and drugs [33]. It is utilized in many applications ranging from scientific research, such as imaging the chiralities of single nanotubes [34] or volcanology [3], to real-world problems involving medical imaging

[35], food analysis, and safety inspection [36, 37], forensic sciences [38, 39], criminology [40], art conservation [41], or agriculture [42].

These applications typically employ the IR spectral region, as each chemical has a particular absorption spectrum in this region. A broad range of application fields leads to extensive research in IR HSI. Compared to the HSI "mainstream," the exploitation of CS in HSI is far more seldom. It focuses mainly on the VIS-NIR spectral region because it is easily manageable in the sense of optical elements and detectors' availability, alignment, etc. The VIS-NIR applications will not be mentioned in this brief summary since we are mainly interested in longer wavelengths.

Our main interest lies in MIR and LWIR, which are commonly used abbreviations for the spectral ranges of 3-8 μm and 8-15 μm, respectively. Note that the delimitation of these ranges slightly varies throughout the literature. To mention a few from the MIR and LWIR spectral regions, Ref. [43] from 2021 provides a proof-of-concept optical setup operating on 3-5 μm, which is able to capture a hyperspectral datacube of 64×48×100 with the acquisition time within one minute. It uses a digital micromirror device (DMD) for spatial encoding, which has to be modified to operate in the MIR spectral region. To the best of my knowledge, this is the only existing work on MIR hyperspectral imaging based on compressed sensing. Regarding LWIR, there are very few publications [44, 45, 46], but note that the list might not be exhaustive. References [44], [45], and [46] all present a LWIR hyperspectral imager using single-pixel detection technology, which collects all three dimensions on a single detection element. However, the experimental results are very limited. To this day, I was not able to find any work regarding LWIR CASSI.

2.4 Objectives

Here we will set the main objectives and goals that triggered the work in this thesis. The overall goal is to localize and distinguish between different chemical substances in the IR spectral region. Therefore, we aim to obtain HSI in a broad spectral range covered with many (up to 100) spectral frames. This is in contrast to previous CASSI reports, which used narrow spectral width and limited spectral resolution. The studied HS camera operating in the VIS spectral range served as a model system for testing the real-life CASSI datacube retrieval and for an outlook of IR CASSI imaging.

This is to be done by keeping the following points:

(1) We aim to retain only one snapshot or, to be more precise, capture all the information in one instance since it is the main advantage of CASSI. Also, we want to keep the optical system as simple as possible, i.e., not using a second detector nor any advanced light modulators.
(2) The demand for reconstructing real-life complex datacubes implies that we need to improve the compression ratio of the measurement.
(3) We aim at using a relatively simple optical system suffering from certain optical aberrations, which can potentially also be created in the IR spectral region.

As we show in the following sections, we reached the set objectives by modifying the optical setup while retaining the simplicity of the system. And more importantly, it leads to a significant improvement in compression ratio and consequently also the retrieved datacube quality. The simulations of our modified setup demonstrate the feasibility of such a system in the IR spectral region.

3 Experimental part: putting it together

The experimental part of this thesis is devoted to the description of our experimental setup, its parameters (including spectral efficiency and aberrations), and the modifications that were necessary to push the limits of the CASSI method. There are also discussed the data processing, calibration, simulations, estimation of an initial guess, and reconstructions that were performed using Matlab. As a reconstruction algorithm, we use TwIST (Two-Step Iterative Shrinkage/Thresholding) [47] for image restoration during the reconstruction.

The following chapters provide a short overview and give more insight into the papers that are a part of this thesis. They constitute an extensive portion of Chapters 4-6. Chapter 7 evaluates the effectiveness of the CASSI extensions made within this work for hyperspectral imaging in the IR spectral region.

4 Evaluation of using standard coded aperture imaging in the IR region

This chapter provides a short overview and more insight into the paper Evaluation of using coded aperture imaging in the mid- and far-infrared region [48].

The central goal of this paper was to test the feasibility of using the standard CASSI method in the IR spectral region. We performed numerous reconstructions of artificial hyperspectral scenes, which included a spill of a chemical agent. Implementation of CASSI operating in the IR would enable less expensive and simpler construction of HSI devices.

The simulations included a simple and complex scene, illumination by black-body radiation, and the effect of noise on the reconstruction quality. Several different sizes of the random mask (32x32 – 512x512 px) were evaluated as well as a different number of spectral slices (117-470) and varying concentrations (100-2000 ppm-m) of the chemical compound. The number of spectral slices reflects the spectral resolution, while varying the concentration impacts the intensity at specific spectral slices in proportion with the absorption spectrum of the chemical.

Throughout Chapter 4, we employed the standard CASSI method.

4.1 Reconstructions

The reconstructions were performed using the TwIST algorithm [47]. It recovers the datacube from the fed detected image, and subsequently, we can extract the absorption spectrum of the chemical agent. In order to correctly determine the chemical agent and its concentration, the relative intensity and position of the peaks are important factors.

4.2 Results and discussion of Chapter 4

We obtained a reasonable agreement between the original and reconstructed spectrum – see Figure S3A. The data shown are for a datacube dimension of 128×128×470. The reconstructed spectra were obtained as a mean value of the central part on the position where the chemical was originally located. From Figure S3D, it can be seen that the highest intensity stripe in the upper part of the original image in Figure S3B was partially restored. We can as well, at a very rough guess, estimate where the chemical compound is located – compare the dark part with Figure S3C. Yet, the resemblance is very coarse, and we cannot talk about any resolution of finer details. It is worth noting that the data shown in Figure S3A-D are without any noise, and even 1% of the noise level (approx. 43.5 dB) added to the detected image seriously impacts the reconstruction (Figure S3E-F).

In other words, our results suggest that the standard CASSI could potentially determine the type of chemical agent and solely roughly localize it only for the ideal case, i.e., without any noise. Therefore, to make CASSI work in the IR spectral region, there is a necessity for an upgrade of the method.

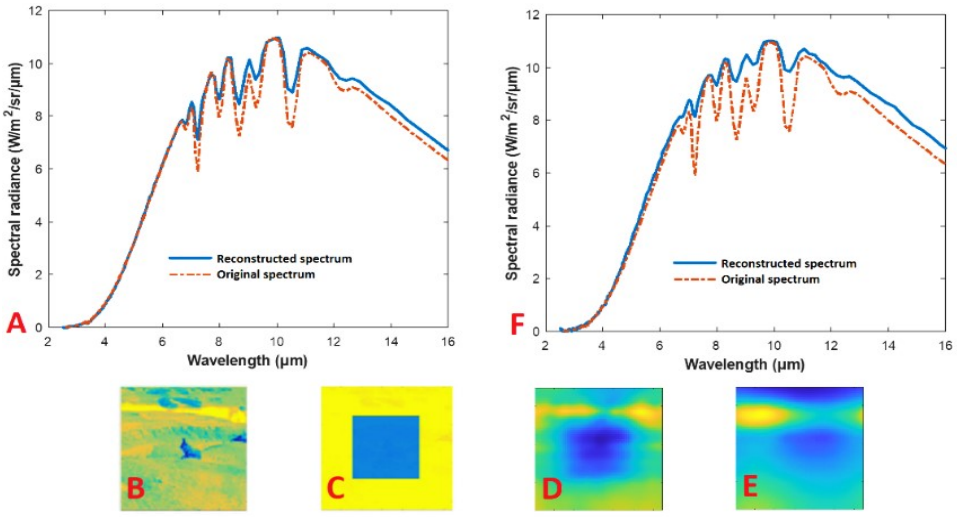

Figure S3 (A) Original (red) and reconstructed (blue) spectra of data without noise. (B) Original scene. (C) A slice of the original datacube with the most prominent absorption in the central part. (D) A slice of the reconstructed datacube without noise. (E) A slice of the reconstructed datacube with 1% of noise. (F) Original (red) and reconstructed (blue) spectra of data with 1% of noise. Adapted from [48]

5 Extension of CASSI by a zeroth-order image

This chapter provides a short overview and more insight into the paper Enhancement of CASSI by a zero-order image employing a single detector. [49]

In order to improve the reconstruction fidelity, there was a need to find a way to gain more information about the measured scene. As mentioned previously (Chapter 2), one way to improve the CASSI method is to capture the non-diffracted image on a second detector [14, 27, 28, 29,30]. However, this modification makes the imaging system more complex, and since it typically includes a beam splitter, it causes a substantial loss of light intensity, which could reach as much as 50% [27].

A significantly better approach to keep the simplicity of the system is to utilize the zeroth-order (ZO) diffraction arising from the diffraction grating. This image is inherently present in the systems employing a diffraction grating, but its use has not been reported for the CASSI experiment. Nevertheless, for the realization of this idea, some changes to the HDES system [50] had to be made – see Chapter 5.1 in the thesis.

The results presented in this chapter, as well as in the paper [49], are derived from the upper image created by the double lens (see Chapter 6 and Figure S6).

5.1 ZO enhanced CASSI measurements

Using our modified CASSI system, we measured several different testing scenes illuminated by a monochromatic light source (Nd:YAG laser, 532 nm), a red diode, or a broadband quartz tungsten-halogen lamp (Thorlabs). In Figure S4, on the left, there is an example of two detector images. The upper one is for

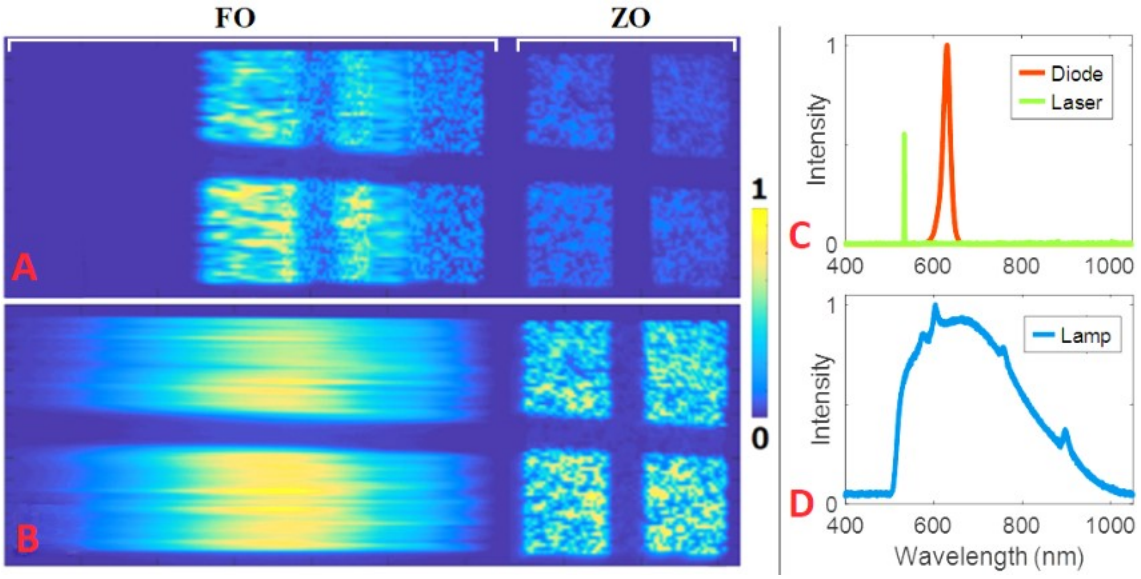

Figure S4 (A) Detector image of an opaque cross illuminated by a green laser and a red diode, and (B) illuminated by a broadband light source. The FO of diffraction is on the left, the ZO of diffraction is on the right. Images resolution is 600×2260 px (C) Measured spectra of the green laser and the red diode, and (D) the broadband light source.

an opaque cross illuminated by a green laser and a red diode, and the bottom one is for the same cross but illuminated by a broadband light source. The spectra of the used light sources are shown in Figure S4C-D. The FO of diffraction is on the left, while the ZO of diffraction is on the right. Note that in the ZO image, a random mask pattern is apparent for both scenes. Whilst in the FO image, it can be identified only for the scene illuminated by green laser light and a red diode – Figure S4A. In this case, the spectral shearing is not so prominent, contrary to a broadband light source – Figure S4B.

5.2 The effect of using the ZO

The TwIST algorithm [47] used for reconstruction enabled us to feed an initial guess (Chapter 3.2.3 in the thesis) of the datacube, so we do not have to start from a trivial guess implemented in the algorithm [49]. We tested the use of the ZO on the quality of the reconstruction by employing the ZO (i) in the initial guess only; (ii) in the reconstruction itself only; (iii) in both the initial guess and the reconstruction; and (iv) without using the ZO at all.

The results summarized in Figure S5 for the cross illuminated with a broadband light show that capturing and utilizing the ZO has a tremendous effect on the spatial quality of the reconstructed datacube. Each quadrant in Figure S5 depicts selected spectral slices at different wavelengths and an overall spectrum of the reconstructed scene for four different approaches to using the ZO image. Panel A shows reconstruction by the standard CASSI method; panel B has a ZO-assisted initial guess along with a standard CASSI reconstruction; panel C comprises using the ZO only in the iterative part of the TwIST

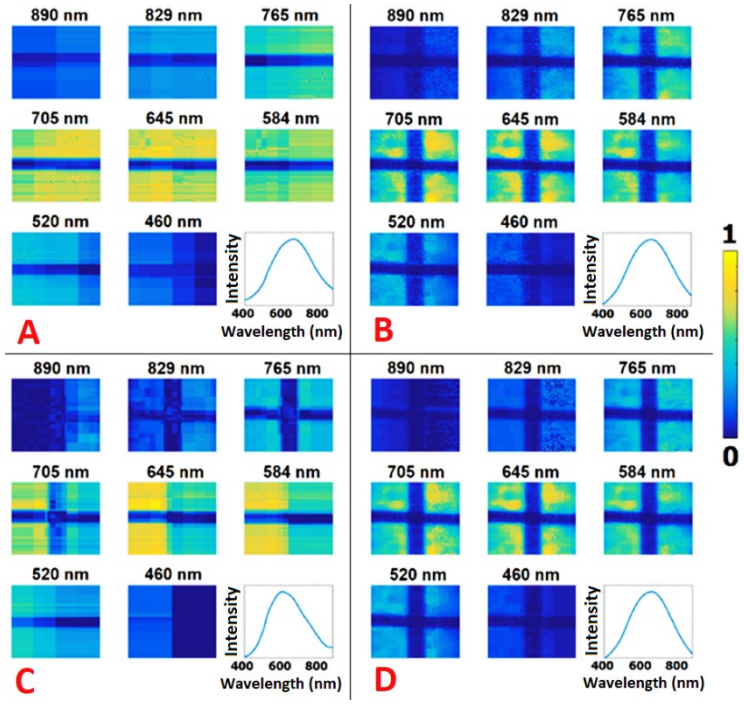

Figure S5 Reconstructions of the scene from Figure S4B; each selected spectral slice is normalized to the maximum datacube value, color bar is on the right. (A) Not using ZO; (B) using ZO in initial guess only; (C) using ZO in operator $\widehat{W}$ only; (D) using ZO both in initial guess and operator $\widehat{W}$. – Adapted from [49]

reconstruction; panel D includes the ZO knowledge in both the initial guess and the datacube reconstruction.

It is noticeable that without using the ZO – Figure S5A, the CASSI method struggles to restore vertical features in the scene. It is caused by spectral shearing (see the FO image in Figure S4B), which significantly diminishes the restoration of the perpendicular lines of the scene. This effect is more prominent for the measurements of broader spectral regions with many spectral slices where the compression ratio is low. Reconstructed datacube slices in Figure S5C show the significance of having a reliable initial guess. The algorithm was not able to restore the opaque cross correctly in all the slices. The use of ZO in the initial guess is highly improving the spatial quality of the reconstructed datacube, as can be seen in Figure S5, panels B and D.

But even for the most accurate reconstruction in Figure S5D, where ZO is used for both the datacube initial guess and retrieval, the overall spectrum below 500 nm does not resemble the actual one. In this spectral region, the intensity should be equal to zero because of the used cut-off filter.

To some extent, the spectral similarity can be enhanced by using a higher regularization parameter τ, which promotes sparsity (see the thesis for details), as we describe in Ref. [49].

5.3 Conclusion of Chapter 5

The presented extension of the CASSI method was constructed with a limited number of optical elements based mainly on off-the-shelf optics. It can be employed for systems exhibiting low compression ratios and suffering from aberrations, especially if there is a need to preserve the system's simplicity. The proposed modification of CASSI is unique in the sense that it enables to capture a spectrally dispersed image of a scene as well as a nondispersed one on the same detector.

We measured different scenes on a broad spectral range (500–900 nm) and observed the effect of including the nondispersed scene image in the reconstruction as well as optimizing the reconstruction parameters. For instance, the regularization parameter τ, which promotes sparsity, has a significant effect on the reconstruction quality. Low values of τ enhance spatial quality, while high values improve spectral similarity.

The modification led to improved overall reconstruction quality and an approximately five-fold reduction in computational time. Note that the improvement of results is not only because of the higher compression ratio but also because of obtaining more spatial information – we can set the initial guess very close to the original scene. These effects are more prominent for complex scenes.

The real data findings were confirmed by simulations (see Chapter 5.4 in the thesis) utilizing rigorous analysis of aberrations, which provided us with quantification of the quality of the results.

6 Extension of CASSI by double projection and differential coded aperture

An important factor limiting the quality of retrieved data via compressed sensing is the so-called compression ratio, i.e., the number of measured data points with respect to the number of elements of the reconstructed dataset. A hyperspectral datacube with dimensions of 64×64×123 px will have a spectrally sheared imprint of 64×186 px on the detector. The compression ratio (CR) is, in this case, 11904/503808 ≈ 2.4%. Using the upgrade from the previous chapter, the CR increases to 16000/503808 ≈ 3.2% since the detector image is now extended by the 64×64 px zeroth order. A significant improvement in the reconstruction quality was achieved. However, the aberrations still limit the reconstruction of complex scenes.

Another way to amplify the performance of CASSI is to take multiple snapshots of the same scene [21, 22, 23]. Yet, in this way, the CASSI system needs some advanced modulator (such as DMD – Digital Micromirror Device) in order to change the random mask pattern. Furthermore, it loses its main advantage of capturing the whole scene in a single instance. Hence, the question is: how to take more snapshots while keeping the simplicity of the system?

A solution is to project the scene in parallel with two lenses through two different random masks at the same time. The proof of concept is presented in the paper Improving Compression Ratio in CASSI [51]. Chapter 6 in the thesis explains in detail the question: how to take more snapshots while keeping the simplicity of the system? Also, the modification of the optical system for double projection and the effect of random mask complementarity are described. Further, simulations confirming the findings of real-data reconstructions are presented along with evaluation metrics of retrieved datacubes for different scenes and utilizing random masks of higher dimensions. At last, a comparison of reconstructions using different algorithms is shown. See the thesis for more details.

6.1 Differential CASSI measurements and approaches to data processing

Chapter 6.3 in the thesis showed that complementary masks are the best option for a double-mask CASSI system. Following these findings, the experimental implementation was carried out only for the complementary random masks. In particular, we used two random binary complementary masks of 64×64 pixels.

An example of such a double-mask measurement can be seen in Figure S6B. It is possible to approach the data reconstruction in several ways compared to the standard multi-snapshot CASSI, owing to the mask's complementarity. We denote the standard multi-snapshot approach as *Double*, which means that the two detector images are optimized during the datacube retrieval in parallel. The standard single-snapshot CASSI is represented in this chapter as *Single*. Nevertheless, in our complementary measurements, we can subtract the upper and the lower image, which would correspond to a measurement with a mask

composed of ±1s – we indicate it as *Diff*. It is worth noting that CS algorithms work better for {+1,-1} matrices than for {+1,0} matrices because of their compressed sensing performance [52].

However, by using only this differential image, we would lose the information about the magnitude – this occurs when one subtracts two similar datasets, which are shifted with respect to each other. Therefore, a better way to process the data is to calculate not only with the difference between the snapshots but also with their sum – the *Diffsum* approach. It is a combination of the differential character of the random mask while it preserves the information about the image intensity scaling. The matrix notations overview of detector images $\overline{D}$ for all the approaches is in Table S1.

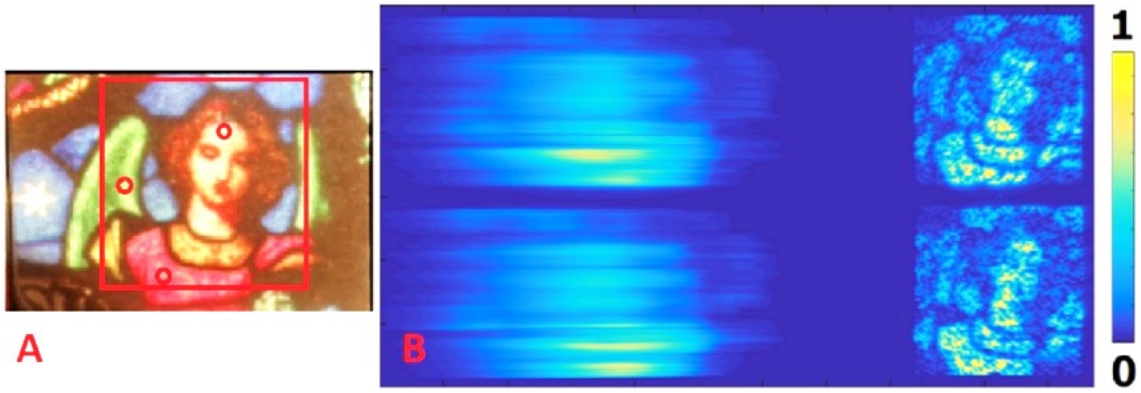

Figure S6 (A) Example of a complex scene with many different spectral features. The red square marks the imaged area. The red circles are used for spectra comparison. (B) The scene from (A) detected by our CASSI system. Note that the same color bar applies to Figure S7 and Figure S8. Addapted from [53]

Table S1: Different approaches to data processing. $\overline{D}$ *denotes detector image.* A *and* B *are upper and lower FO images, respectively.*

Data processing approach	*Matrix notation*
Single	$\overline{D} = [A]$
Double	$\overline{D} = [A; B]$
Diff	$\overline{D} = [A - B]$
Diffsum	$\overline{D} = [A - B; A + B]$

The final detector image D fed to the reconstruction algorithm is $D = [\overline{D}\ \overline{ZO}]$, where $\overline{ZO}$ is a sum of upper and lower ZO images.

6.2 The effect of data processing approaches

Here, we will demonstrate the difference between the data processing approaches on two scenes – an opaque cross and a stained glass foil illuminated by a spectrally broad light. More examples can be found in Ref. [53]. Figure S7 shows selected slices of the reconstructed datacube for different data processing approaches. As can be seen, all approaches are able to reconstruct spatial information well since we employ the ZO image in all the cases. Nevertheless, the approaches differ mainly in the reconstructed spectrum of the light. The *Single*, *Diff,* and *Double* approaches face a problem with spectrum reconstruction below 500

nm, where the intensity should be zero due to the use of the yellow cut-off filter. In terms of the reconstructed spectrum, we can safely say that *Diffsum* is the best approach.

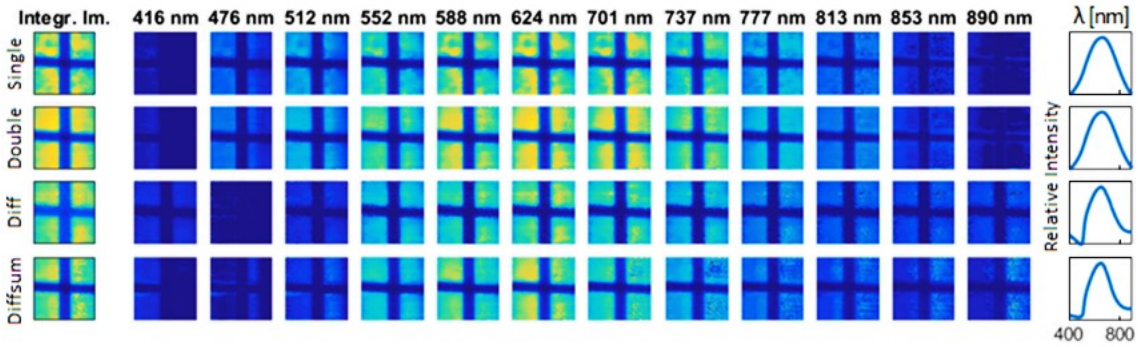

Figure S7 Reconstructed spectrally integrated image, individual spectral slices, and a spectrum of an opaque cross illuminated with broadband light by using four processing approaches (see Table S1). Adapted from [53]

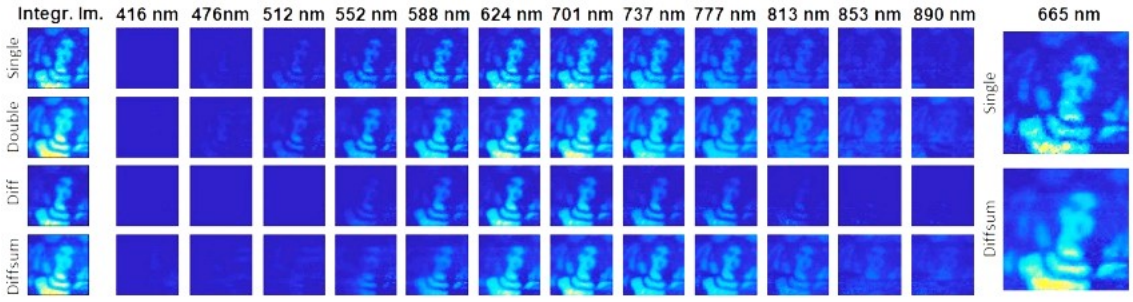

Figure S8 Reconstructed spectrally integrated image and individual spectral slices of an stained glass foil with broadband light by using four processing approaches (see Table S1). Two spectral slices of Single and Diffsum were enlarged for comparison. Extracted from [53]

To show the ability of the system to retrieve more complex scenes, we performed measurements of a stained glass foil (see the scene in Figure S6). It is worth noting that the good spatial information obtained is mainly thanks to the extension of CASSI by the ZO image, which was described in the previous chapter. Nevertheless, we can see the improvement as we extend into the double mask approaches, which exhibit much better homogeneity compared to the *Single* approach. See the selected enlarged slices in Figure S8 for comparison. It shows that *Diffsum* exhibit more uniformity as opposed to *Single*.

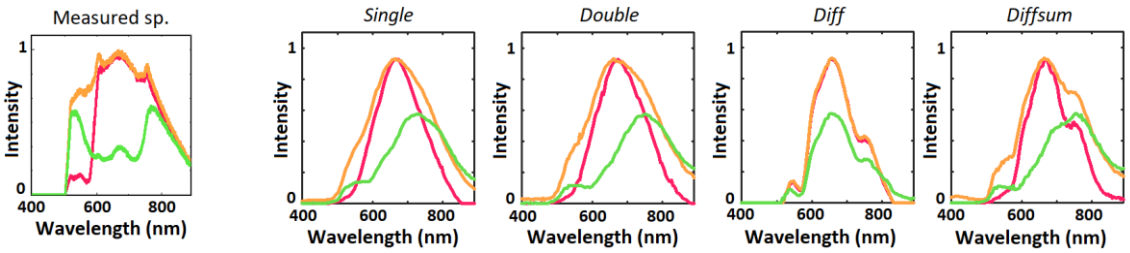

Figure S9 Measured spectra at the points marked in Figure S6A (on the left). Reconstructed spectra at the same points for four different reconstruction approaches (on the right).

In Figure S9 are depicted the measured and reconstructed spectra of three points of the stained glass foil scene. The colors of the curves correspond to the colors of the selected points in the scene. The

results indicate that, although obtaining a good spatial resolution was possible, the scene is too complex to reconstruct spectra reliably. It is worth noting that the spectra were not adjusted for the spectral efficiency of the system. Nevertheless, the closest similarity was achieved using *Diffsum*.

6.3 Conclusion of Chapter 6

We showed that by a simple modification of the optical setup, we were able to improve the compression ratio in CASSI systems 2-fold and as much as 2.7-fold using also the ZO image compared to the standard CASSI. Simultaneously, the modification retained the CASSI's main advantage – a single snapshot.

We demonstrated the improvement in the reconstruction quality on a broad spectral range of 500-900 nm. Utilizing the *Double* approach, which is equivalent to multi-snapshot CASSI, it reached an increase of ~1.0 dB in PSNR. We also quantified the superiority of complementary masks over noncomplementary ones. With the use of the ZO image, we were able to make the initial estimate of the datacube very similar to the measured scene, which, on average, decreased the total number of reconstruction iterations needed.

Moreover, we proposed a new approach to data processing which we denoted as *Diffsum* or differential CASSI (D-CASSI) since it utilizes a matrix of {+1,-1} as a random mask. This was possible thanks to the mask's complementarity. PSNR, in this case, soared ~1.9 dB compared to *Single*.

We backed our measurement of real scenes with rigorous simulations, which enabled us to quantify the results. It also allowed us to control the reconstruction parameters better, explore the possibility of using different reconstruction algorithms, compare our proposed approach to standard CASSI covering the whole double projection area, and investigate utilizing random masks of higher dimensions.

7 Evaluation of the CASSI extensions in the IR region

The ultimate goal of the thesis was to evaluate the effectiveness of the CASSI extensions made within this work for hyperspectral imaging in the IR spectral region. Therefore, we created a set of artificial scenes and detector images as it would be produced by an IR CASSI system. As opposed to the visible spectral region, it is also necessary to consider the radiation of a black body, which could be calculated by Planck's law – see Chapter 1.1.1 in the thesis. Compared to Chapter 4, here we implemented both extensions of CASSI, which shift the abilities of the method to a different level.

The random mask dimensions in our optical setup were constrained by the aberrations present in our system, as it was designed mainly on off-the-shelf optics due to the vision of building an analogous setup in the IR. However, the results for higher resolution masks in Ref. [53] showed that using a 256×256 px random mask would lead to better CASSI performance. Therefore, we exploited this knowledge and used it in the following simulations. There is also a practical rule mentioned in Ref. [54], which says that for exact recovery, it is necessary to have about four incoherent samples per unknown nonzero term. I.e., the number of samples is equal to 4 times the sparsity level. It also underlines the idea behind using a higher-resolution mask.

This chapter describes data preparation, reconstruction and scene parameters testing, the noise and spectral dimension size effect, and various approaches to improve hyperspectral data reconstruction (e.g., promoting sparse solutions via multiple regularization weights). Finally, results combining spectrally-focused reconstruction with a zeroth-order image are shown.

7.1 Reconstruction and scene parameters testing

First, a set of different parameters were tested on a datacube 256×256×50 with distinct properties to identify the major parameters to tune during the optimization of datacube retrieval. The tested parameters and scene properties included:

- Noise in the detected image with a different amount of SNR in dB (23.5, 34.8, 44.8, and without noise)
- The concentration of the chemical agent (isopropanol of 1000 ppm-m or 3333 ppm-m)
- Transforming the spectral slices with various wavelet transforms (Haar and Symlet 8)
- Option to use DCT (discrete cosine transform) of the datacube in the spectral dimension
- Different values of regularization parameter tau (put stress on the sparsity).

The reconstructions that showed the best PSNR results for noisy data were achieved using Symlet 8 wavelets together with DCT in spectral dimension. The results of noisier data were more prominent to be tau dependent. The maximal difference of PSNR between the best results achieved using different tau was 1.9 dB. The most significant reconstruction quality change was observed between SNR 23.5 dB and 34.8 dB. Hence, the next logical step was to create data with finer SNR division around those values.

7.2 Combining spectrally- and spatially-oriented reconstructions

After many trials of improving and enhancing reconstruction quality mentioned in the chapters above, we ended up with two sets of datacube reconstruction parameters – one with a focus on good spatial information (indicated as $SET_{spatial}$) and the other one with a focus on yielding correct spectra (indicated as $SET_{spectral}$). Below we present results for three scenes denoted as Scene A – Figure S10A, Scene B – Figure S10B, and Scene C – Figure S10C [55, 56]. The properties of the data in this chapter were set as follows: datacube 256×256×50 px, the concentration of isopropanol in the scene 1000 ppm-m, noise at the detector SNR = 29.8 dB.

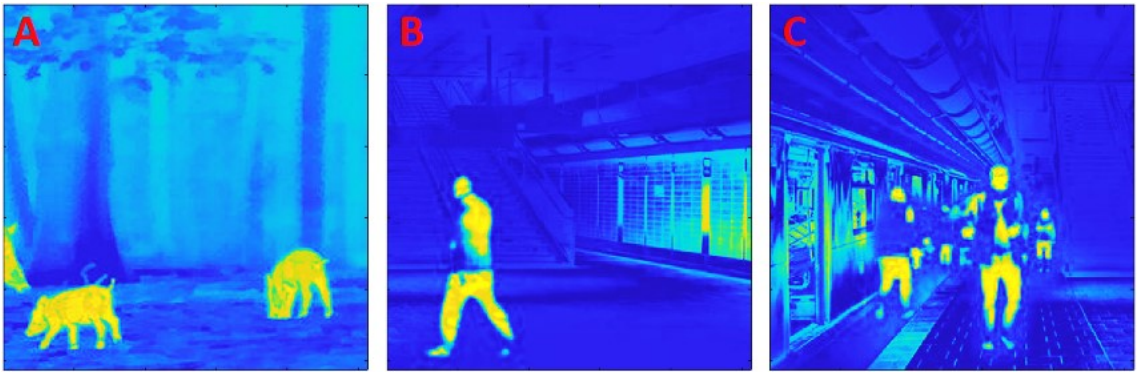

Figure S10 Original scenes used for testing in Chapter 7 denoted as (A) Scene A, (B) Scene B, and (C) Scene C.

One of the important points in evaluating the simulations was the assessment of spectral quality. We found out that the overall SAM score (see Chapter 1.5 in the thesis) does not necessarily reflect the fidelity of the reconstructed spectra of the chemical. Hence, we also considered the mean SAM score only from the area where the chemical is present – we denote it SAM_{chem}. This metric reflects much more faithfully the quality of the retrieved spectral features in the IR region.

This discrepancy can be seen in Table 5 in the thesis, providing the results of Scene A reconstructions. The reconstruction $RecA_{spatial}$ was performed using $SET_{spatial}$, while $RecA_{spectral}$ was reconstructed using $SET_{spectral}$. $RecA_{spatial}$ achieved a better SAM score than $RecA_{spectral}$, but at the same time, SAM_{chem} is much worse.

The main distinction between the two abovementioned sets of parameters is the use of DCT in the spectral dimension. This way, DCT highly promotes correct spatial information but corrupts the spectra. The evaluation metrics of these reconstructions are in Table 5 in the thesis, denoted as $RecA_{spatial}$ and $RecA_{spectral}$, respectively. It can be seen that $RecA_{spatial}$ is superior in terms of spatial correctness (higher PSNR and SSIM), but the spectra in points P3-P5 are absolutely missing spectral features of the spilled chemical (higher spectral error SAM_{chem}). In contrast, for $RecA_{spectral}$, we obtain more reliable spectra, but the reconstructed images resemble seeing the scene with severe myopia (see Figure 30 in the thesis).

From this point of view, it is not possible to obtain accurate spatial and spectral information at the same time. Nevertheless, considering that our primary goal is to localize and identify a chemical compound in a scene, we should prioritize the faithful spectra. Here comes into play, once again, the invaluable feature

of our system that arises from the combination of CASSI extensions described in Chapters 5 and 6 in the thesis – i.e., acquiring a zeroth-order image of a scene.

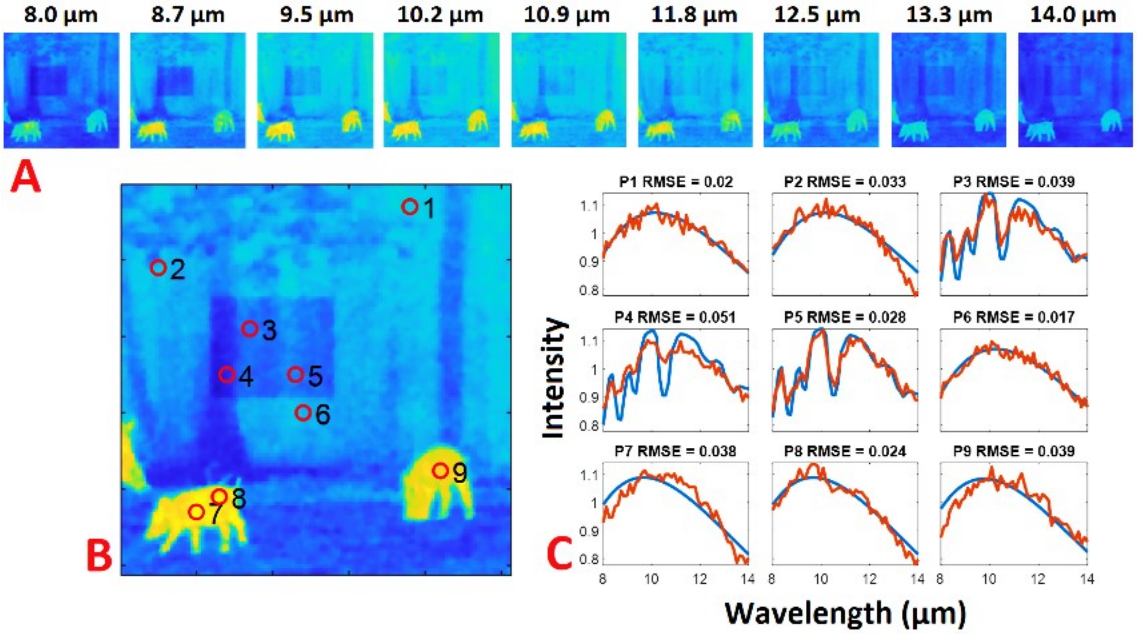

Figure S11 The best achievable results for Scene A using a combination of $SET_{spectral}$ and post-reconstruction utilization of zeroth-order image according to Equation S1. The reconstruction is denoted as $RecA_{comb}$. (A) Selected reconstructed slices. (B) Integrated reconstructed slices. (C) Original (blue) and reconstructed (red) spectra from the points marked in B.

We know that the ZO image has correct spatial information as it is an integral combination of all encoded slices of the measured datacube. Hence, by scaling each spectrum according to the corresponding pixel intensity in the ZO, we preserve the spectra while achieving great spatial resolution. It can be written as:

$$\mathrm{DC}(i,\mathrm{j},\lambda) = DC_{Norm}(i,j,\lambda)\,.\,ZO(i,j) \qquad \textit{Equation S1}$$

where $DC_{Norm}(i,j,\lambda)$ is the reconstructed datacube normalized on its mean value, $ZO(i,j)$ is the zeroth-order image, and $\mathrm{DC}(i,\mathrm{j},\lambda)$ is the resulting datacube.

Performing $SET_{spectral}$ reconstruction and then applying Equation S1 to the reconstructed datacube, we obtain results in Figure S11, which clearly outperform the reconstructions $RecA_{spatial}$ and $RecA_{spectral}$ – see $RecA_{comb}$ for comparison in Table 5 in the thesis. In Figure S11, there are selected reconstructed spectral slices (panel A), an integrated image of all the reconstructed slices (panel B), and spectra from nine selected points P1-P9 of the scene (panel C). The location of the points can be seen in panel B. The same applies to Figure S12 and Figure S13.

Table S2: The best achievable results for a combination of $SET_{spectral}$ and post-reconstruction utilization of ZO image according to Equation S1 for Scene A-C

	PSNR	SSIM	SAM	SAM_{chem}
$RecA_{comb}$	34.63	0.90	1.35	2.24
$RecB_{comb}$	34.41	0.90	1.41	2.22
$RecC_{comb}$	32.56	0.85	1.56	2.28

In order to evaluate how the reconstruction quality would change in dependence on different conditions, we tested the reconstruction parameters on different scenes – see Figure S12, Table S2 for results of a scene with a more complicated area of chemical absorption (Scene B, Figure S10B), and Figure S13, Table S2 for results of a scene with a more complicated area of chemical absorption and more complex spatial features (Scene C, Figure S10C).

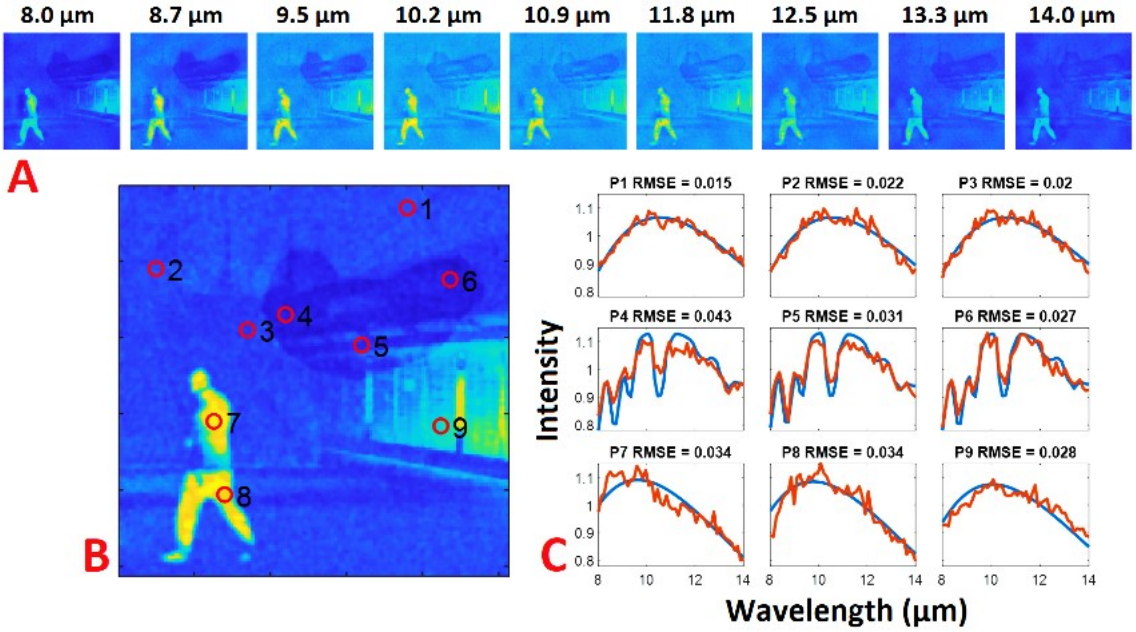

Figure S12 The best achievable results for scene B using a combination of $SET_{spectral}$ and post-reconstruction utilization of zeroth-order image according to Equation S1. The reconstruction is denoted as $RecB_{comb}$. (A) Selected reconstructed slices. (B) Integrated reconstructed slices. (C) Original (blue) and reconstructed (red) spectra from the points marked in B.

Points with higher intensity in the original scene lead to worse quality of reconstructed spectra in these points – see points P7 and P8 compared to points P1 and P2 in Figure S11, Figure S12, and Figure S13. The fine details in the reconstructed slices deteriorated, which is caused mainly due to the noise.

Nevertheless, the degree of retrieved details is more than satisfactory in terms of imaging a scene and locating a chemical substance. Joint reconstructions yielded the same SSIM as reconstructions using $SET_{spatial}$, as well as the same SAM and SAM_{chem} scores as $SET_{spectral}$. PSNR slightly decreased for Scene A and improved for Scene B and Scene C.

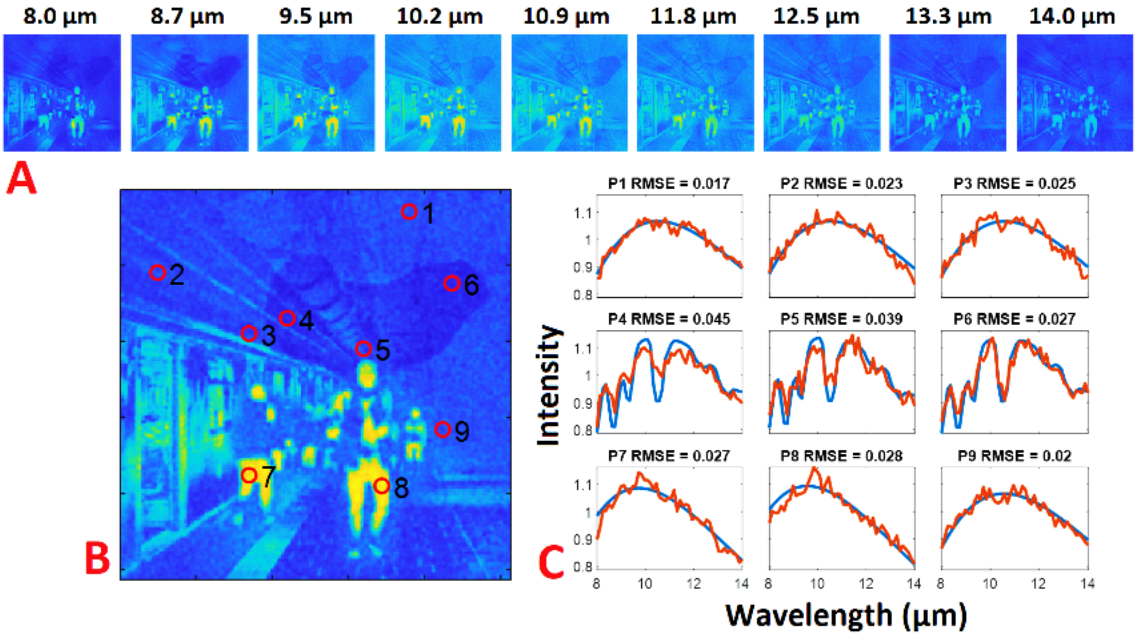

Figure S13 The best achievable results for scene C using a combination of $SET_{spectral}$ and post-reconstruction utilization of zeroth-order image according to Equation S1. The reconstruction is denoted as $RecC_{comb}$. (A) Selected reconstructed slices. (B) Integrated reconstructed slices. (C) Original (blue) and reconstructed (red) spectra from the points marked in B.

7.3 Robustness against noise for the combined retrieval

A good indication of the performance of the system would be to assess the highest amount of noise at which it can still achieve reliable reconstruction. For this purpose, reconstructions of data with varying noise were performed. The regularization parameter tau was set to 0.1 as it consistently provided the best results for all the scenes. Moreover, in a real scenario, tuning this parameter without prior knowledge of the scene would not be possible. The results are summarized in Table S3.

Table S3 Results for Scene C achieved by using a combination of $SET_{spectral}$ and post-reconstruction utilization of ZO image according to Equation S1 with fixed regularization parameter `tau` *for different amounts of noise*

SNR (dB)	PSNR (dB)	SSIM	SAM (°)	SAM_{chem} (°)
34.8	32.65	0.87	1.44	2.26
29.8	32.34	0.86	1.55	2.33
25	30.89	0.79	1.95	2.58
20	28.23	0.67	2.69	3.34
18	26.30	0.57	3.36	3.82
15	23.38	0.43	4.45	5.23

Figure S14 shows that the dependency of reconstruction quality on noise is not linear for both PSNR and SAM_{chem}. From this point of view, an inflection point from which the quality deteriorates rather quickly is near 25 dB of SNR. Hence, the reconstructed data with the noise of 25 dB and 20 dB are presented

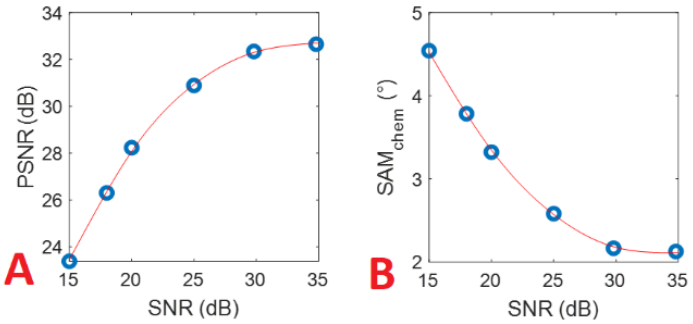

Figure S14 Dependency between SNR of the data and reconstructed (A) PSNR and (B) SAM_{chem}. Plotted data from Table S3, fitted by spline.

in Figure S15A and Figure S15B, respectively. These values translate to 6.4% and 11.3%, respectively. It is still possible to distinguish the spatial information in Figure S15B, even though it is visibly noisier. However, evaluating the spectral information would be a problem as the spectra are severely disrupted. SAM and SAM_{chem}, in this case, surged from 1.95 and 2.58 to 2.69 and 3.34, which is approximately 38% and 30% increase, respectively. We can draw a conclusion that in order to obtain a reliable reconstruction, the maximal SNR in the detected image needs to reach 25 dB.

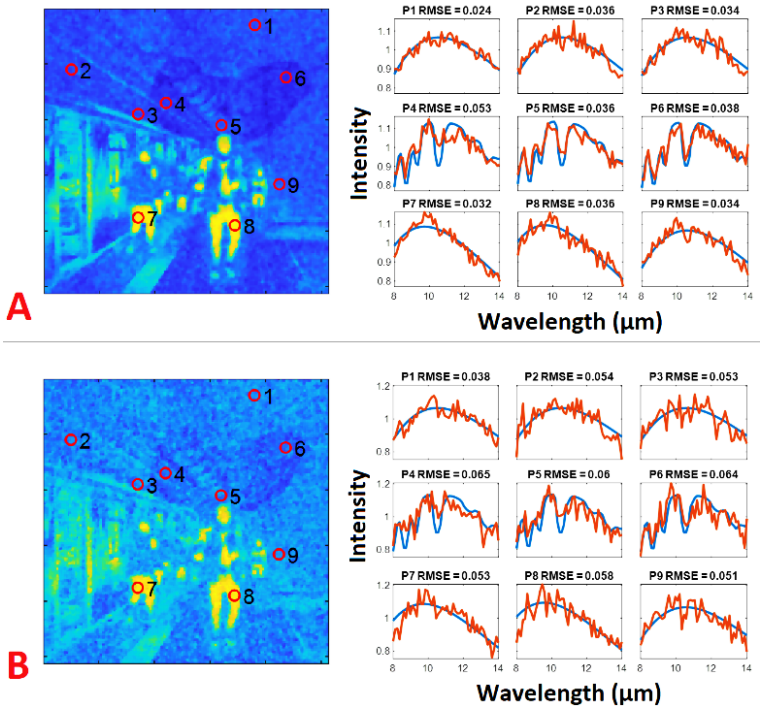

Figure S15 Results for Scene C achieved by using a combination of $SET_{spectral}$ and post-reconstruction utilization of ZO image according to Equation S1 with fixed regularization parameter `tau` *for noise of (A) 25 dB and (B) 20 dB.*

8 Conclusions

Throughout this thesis, we have seen how the compressed sensing (CS) technique CASSI relying on a single snapshot, is a unique aspirant in the field of hyperspectral imaging (HSI). It has enormous potential for obtaining chemical information remotely. Yet, the method possesses a lot of room for improvement. There are two main reasons for this. First, it dismantles the primary disadvantages of HSI, which are halting more widespread use of HS cameras – these are cost and complexity. As was shown in this thesis, CASSI can be constructed as a relatively simple optical setup. Second, CASSI allows capturing HS information at a rate not comparable to any other mean. The increasing research interest in snapshot HSI in recent years is a hint at the potential of these devices, but because of manufacturing limitations, it has not seen wider adoption in commercial use. One exception is the professional astronomical community, which highly benefits from the vast light throughput of a telescope when conducting HSI [57].

The main contribution of this work is that it determined the limiting factors of CASSI – namely, very high compression of the measured data, which is even more pronounced for datacubes with many spectral slices. We proposed and realized extensions needed to overcome the obstacles and then provided a conceptual study of CASSI operating in the LWIR spectral region, which can perform detection and localization of a chemical substance in noisy conditions.

We developed a differential CASSI (D-CASSI) using two complementary binary random masks and, thus, two imaging paths to multiply the measured information and consequently lift the limits of the compression. On top of that, this system combines a diffraction grating and a prism as a dispersive element allowing for concentric mounting. It is designed so that it can capture both the first- and zeroth-order diffraction of the grating on the same detector. Utilizing the zeroth order improves the spatial quality of the reconstructed data dramatically. It is worth noting that thanks to masks' complementarity, we were able to develop a completely new approach to data processing and reconstruction, which utilizes a random mask consisting of {-1,+1} pixels. The synergy of the CASSI extensions brought into existence gives rise to post-reconstruction processing that has a huge positive impact on reconstruction fidelity.

It can be concluded that the modified CASSI system makes it, indeed, possible to perform HSI on a broad spectral range in the IR spectral region in order to localize a chemical substance if the resulting SNR on the detector is at least 25 dB. Note that the made CASSI extensions retained the simplicity of the optical system and the main advantage of CASSI, which is a single-snapshot operation regime.

Comment on the papers

The publications listed below are a part of this thesis. They constitute a substantial portion of Chapters 4-6 and contain information about the experimental design of the presented optical system, altogether with additional results. An interested reader is referred to the following pages, where they are enclosed.

I. HLUBUČEK, J., ŽÍDEK, K.: Evaluation of using coded aperture imaging in the mid- and far-infrared region. In: *5th International Workshop on Compressed Sensing applied to Radar, Multimodal Sensing, and Imaging (CoSeRa)*, Eurasip, 2018. 19.
II. HLUBUČEK, J., et al. Improving Compression Ratio in CASSI. In: *Computational Optical Sensing and Imaging*. Optical Society of America, 2021. CTh2F.3.
III. HLUBUČEK, J., et al. Enhancement of CASSI by a zero-order image employing a single detector. *Applied Optics*. 2021, **60**(5), 1463-1469.
IV. HLUBUČEK, J., et al. Differential coded aperture single-snapshot spectral imaging. *Optics Letters*. 2022, **47**(9), 2342-2345.

The work in Chapter 7 is yet to be published.

My contribution to the papers

In papers **I**-**IV,** I performed the predominant part of the experimental work and all the data analysis. I wrote papers **I**-**IV** with supervision by Karel Žídek.

On behalf of the co-authors, the above-mentioned declaration was confirmed by

Doc. RNDr. Karel Žídek, Ph.D.

References

[1] MANLEY, M. Near-infrared spectroscopy and hyperspectral imaging: Non-destructive analysis of biological materials. *Chemical Society Reviews*. 2014, **43**(24), 8200–8214.
[2] TÜRKER-KAYA, S., HUCK, Ch. W. A Review of Mid-Infrared and Near-Infrared Imaging: Principles, Concepts and Applications in Plant Tissue Analysis. *Molecules*. 2017, **22**(1), 168.
[3] GABRIELI, A., WRIGHT, R., LUCEY, P.G., PORTER, J.N., GARBEIL, H., PILGER E. a WOOD, M. Characterization and initial field test of an 8–14 μm thermal infrared hyperspectral imager for measuring SO2 in volcanic plumes. *Bulletin of Volcanology*. 2016, **78**(10).
[4] ROSI, F., MILIANI, C., BRAUN, R., HARIG, R., SALI, D., BRUNETTI, B.G. a SGAMELLOTTI, A. Noninvasive Analysis of Paintings by Mid-infrared Hyperspectral Imaging. *Angewandte Chemie International Edition*. 2013, **52**(20), 5258-5261.
[5] CALVINI, R., ULRICI, A. a AMIGO, J.M. Practical comparison of sparse methods for classification of Arabica and Robusta coffee species using near infrared hyperspectral imaging. *Chemometrics and Intelligent Laboratory Systems*. 2015, **146**, 503-511.
[6] CANDES, E.J. a WAKIN, M.B. An Introduction To Compressive Sampling. *IEEE Signal Processing Magazine*. 2008, **25**(2), 21-30.
[7] DONOHO, D.L. Compressed sensing. *IEEE Transactions on Information Theory*. 2006, **52**(4), 1289-1306.
[8] TAYLOR, H. L., BANKS, S. C., MCCOY, J. F. Deconvolution with the ℓ 1 norm. *Geophysics*. 1979, **44**(1), 39-52.
[9] HAYES, B. Computing Science: The Best Bits. *American scientist*. 2009, **97**(4), 276-280. https://www.jstor.org/stable/27859352.
[10] WANG, P., LIANG, J. a WANG, L. V. Single-shot ultrafast imaging attaining 70 trillion frames per second. *Nature Communications*. 2020, **11**(1).
[11] BRADY, D.J. *Optical Imaging and Spectroscopy*. Hoboken, NJ, USA: John Wiley & Sons, 2009.
[12] WAGADARIKAR, A., JOHN, R., WILLETT, R. a BRADY, D.J. Single disperser design for coded aperture snapshot spectral imaging. *Applied Optics*. 2008, 47(10).
[13] ARCE, G. R., BRADY, D. J., CARIN, L., ARGUELLO, H., KITTLE, D. S. Compressive Coded Aperture Spectral Imaging: An Introduction. *IEEE Signal Processing Magazine*. 2014, **31**(1), 105-115.
[14] WANG, L., XIONG, Z., GAO, D., SHI, G. a WU, F. Dual-camera design for coded aperture snapshot spectral imaging. *Applied Optics*. 2015, **54**(4).
[15] AMIGO, J. M. Practical issues of hyperspectral imaging analysis of solid dosage forms. Analytical and Bioanalytical Chemistry. 2010, **398**(1), 93-109.
[16] AVIRIS - Airborne Visible / Infrared Imaging Spectrometer. 2022. *AVIRIS Data Portal - JPL - NASA*. [online] Available at: https://aviris.jpl.nasa.gov/dataportal [Accessed 12 October 2022].
[17] CHANG, N. B., VANNAH, B., YANG, Y.J. Comparative sensor fusion between hyperspectral and multispectral satellite sensors for monitoring microcystin distribution in Lake Erie. *IEEE Journal of Selected Topics in Applied Earth Observations and Remote Sensing*. 2014, **7**(6), 2426-2442.
[18] GAO, L., LIANG, J., LI, Ch. a WANG, L. V. Single-shot compressed ultrafast photography at one hundred billion frames per second. *Nature*. 2014, **516**(7529), 74-77.
[19] JACQUINOT, P. The luminosity of spectrometers with prisms, gratings, or Fabry-Perot etalons. *Journal of the Optical Society of America*. 1954, **44**(10), 761-765.
[20] HAGEN, N. A., et al. Snapshot advantage: a review of the light collection improvement for parallel high-dimensional measurement systems. *Optical Engineering*. 2012, **51**(11), 111702.
[21] KITTLE, D., et al. Multiframe image estimation for coded aperture snapshot spectral imagers. *Applied optics*. 2010, 49.36: 6824-6833.
[22] WU, Y., et al. Development of a digital-micromirror-device-based multishot snapshot spectral imaging system. *Optics letters*. 2011, **36(**14), 2692-2694.
[23] ARGUELLO, H, ARCE, G. R. Code aperture optimization for spectrally agile compressive imaging. *Journal of the Optical Society of America A*. 2011, **28(**11), 2400-2413.
[24] ARGUELLO, H., ARCE, G. R. Rank minimization code aperture design for spectrally selective compressive imaging. *IEEE transactions on image processing*. 2012, **22(**3), 941-954.
[25] ARGUELLO, H., ARCE, G. R. Code aperture design for compressive spectral imaging. In: *2010 18th European Signal Processing Conference*. IEEE, 2010. 1434-1438.

[26] ARGUELLO, H., et al. Higher-order computational model for coded aperture spectral imaging. *Applied optics*. 2013, **52(**10), D12-D21.
[27] YUAN, X., TSAI, T. H., ZHU, R., LLULL, P., BRADY, D. J., CARIN, L. Compressive Hyperspectral Imaging With Side Information. *IEEE Journal of Selected Topics in Signal Processing*. 2015, **9**(6), 964-976.
[28] WANG, L., XIONG, Z., SHI, G., ZENG, W. a WU, F. Compressive hyperspectral imaging with complementary RGB measurements. *Visual Communications and Image Processing (VCIP)*. IEEE, 2016. 1-4.
[29] RUEDA, H., ARGUELLO, H., ARCE, G. R. Dual-ARM VIS/NIR compressive spectral imager. In: *2015 IEEE International Conference on Image Processing (ICIP)*. IEEE, 2015. 2572-2576.
[30] WANG, L., et al. High-speed hyperspectral video acquisition with a dual-camera architecture. In: *Proceedings of the IEEE Conference on Computer Vision and Pattern Recognition*. IEEE, 2015. 4942-4950.
[31] WAGADARIKAR, A. A., et al. Video rate spectral imaging using a coded aperture snapshot spectral imager. *Optics express*. 2009, **17(**8), 6368-6388.
[32] FENG, Y. Z., SUN, D. W., Application of Hyperspectral Imaging in Food Safety Inspection and Control: A Review. *Critical Reviews in Food Science and Nutrition*. 2012, **52**(11), 1039-1058.
[33] GENDRIN, C., ROGGO, Y., COLLET, C. Pharmaceutical applications of vibrational chemical imaging and chemometrics: A review. *Journal of Pharmaceutical and Biomedical Analysis*. 2008, **48**(3), 533–553.
[34] ROXBURY, D., et al. Hyperspectral microscopy of near-infrared fluorescence enables 17-chirality carbon nanotube imaging. *Scientific reports*. 2015, **5**(1), 1-6.
[35] CARRASCO, O., et al. Hyperspectral imaging applied to medical diagnoses and food safety. In: *Geo-Spatial and Temporal Image and Data Exploitation III*. SPIE, 2003. 215-221.
[36] CALVINI, R., ULRICI, A., AMIGO, J. M. Practical comparison of sparse methods for classification of Arabica and Robusta coffee species using near infrared hyperspectral imaging. *Chemometrics and Intelligent Laboratory Systems*, 2015. **146**, 503-511.
[37] FENG, Y. Z., SUN, D. W. Application of hyperspectral imaging in food safety inspection and control: a review. *Critical reviews in food science and nutrition*, 2012. **52**(11) 1039-1058.
[38] EDELMAN, G.J., GASTON, E., VAN LEEUWEN, T.G., CULLEN, P.J. a AALDERS, M.C.G. Hyperspectral imaging for non-contact analysis of forensic traces. *Forensic Science International*. 2012, **223**(1-3), 28-39.
[39] SCHULER, R. L., KISH, P. E., PLESE, C. A. Preliminary observations on the ability of hyperspectral imaging to provide detection and visualization of bloodstain patterns on black fabrics. *Journal of forensic sciences*, 2012. **57(**6), 1562-1569.
[40] PEREIRA, J. F. Q., et al. Detection and identification of Cannabis sativa L. using near infrared hyperspectral imaging and machine learning methods. A feasibility study. *Spectrochimica Acta Part A: Molecular and Biomolecular Spectroscopy*, 2020. **237,** 118385.
[41] BALAS, C., et al. Hyperspectral imaging and spectral classification for pigment identification and mapping in paintings by El Greco and his workshop. *Multimedia Tools and Applications*, 2018. **77**(8), 9737-9751.
[42] MAHESH, S., JAYAS, D.S., PALIWAL, J. a WHITE, N.D.G. Hyperspectral imaging to classify and monitor quality of agricultural materials. *Journal of Stored Products Research*. 2015, **61**, 17-26.
[43] YANG, S., et al. Mid-infrared compressive hyperspectral imaging. *Remote Sensing*, 2021. **13(**4), 741.
[44] RUSSELL, T. A., et al. Compressive hyperspectral sensor for LWIR gas detection. In: *Compressive Sensing*. SPIE, 2012. 55-67.
[45] DUPUIS, J. R., KIRBY, M., COSOFRET, B. R. Longwave infrared compressive hyperspectral imager. In: *Next-Generation Spectroscopic Technologies VIII*. SPIE, 2015. 232-242.
[46] CRAIG, Stephanie M., et al. Compressive sensing hyperspectral imager in the LWIR for chemical plume detection. In: *Algorithms, Technologies, and Applications for Multispectral and Hyperspectral Imaging XXVIII*. SPIE, 2022. 186-199.
[47] BIOUCAS-DIAS, J. M., FIGUEIREDO, M. A. T. A New TwIST: Two-Step Iterative Shrinkage/Thresholding Algorithms for Image Restoration. *IEEE Transactions on Image Processing*. 2007, **16**(12), 2992-3004.
[48] HLUBUČEK, J., ŽÍDEK, K.: Evaluation of using coded aperture imaging in the mid- and far-infrared region. In: *5th International Workshop on Compressed Sensing applied to Radar, Multimodal Sensing, and Imaging (CoSeRa)*, Eurasip, 2018. 19.
[49] HLUBUČEK, J., et al. Enhancement of CASSI by a zero-order image employing a single detector. *Applied Optics*. 2021, **60(**5), 1463-1469.

[50] ŽÍDEK, K., DENK, O., HLUBUČEK, J. a VÁCLAVÍK, J. Compact and robust hyperspectral camera based on compressed sensing. In: *Optics and Measurement International Conference 2016*. SPIE, 2016. 165-171.
[51] HLUBUČEK, J., LUKEŠ, J., ŽÍDEK, K. Improving Compression Ratio in CASSI. In: *Computational Optical Sensing and Imaging*. Optical Society of America, 2021. CTh2F.3.
[52] SOLDEVILA, F., et al. Use of balanced detection in single-pixel imaging. In: *Computational Optical Sensing and Imaging*. Optica Publishing Group, 2016. CW5D.5.
[53] HLUBUČEK, J., et al. Differential coded aperture single-snapshot spectral imaging. *Optics Letters*. 2022, **47**(9), 2342-2345.
[54] CANDÈS, E. J., ROMBERG, J., TAO, T. Robust uncertainty principles: Exact signal reconstruction from highly incomplete frequency information. *IEEE Transactions on information theory*, 2006. **52(**2), 489-509.
[55] Euregiohunt. 2022. *Calonox View*. [online] Available at: https://cdn.webshopapp.com/shops/215633/files/360391341/leica-calonox-view.jpg [Accessed 12 October 2022].
[56] Leica geosystems. 2022. *LiDAR Based Security Solutions - Leica BLK247*. [online] Available at: https://shop.leica-geosystems.com/sites/default/files/styles/gallery_medium/public/2020-11/BLK247_Subway_IR_view.jpg [Accessed 12 October 2022].
[57] HAGEN, N. A., et al. Snapshot advantage: a review of the light collection improvement for parallel high-dimensional measurement systems. *Optical Engineering*, 2012. **51(**11), 111702.